

## Supporting Information

### to Accompany

#### Electronic Structure of Nickel(II) and Zinc(II) Borohydrides from Spectroscopic Measurements and Computational Modeling

Patrick J. Desrochers,<sup>a,\*</sup> Christopher A. Sutton,<sup>a</sup> Micah L. Abrams,<sup>b</sup> Shengfa Ye,<sup>c</sup> Frank Neese,<sup>c</sup>

Joshua Telser,<sup>d,\*</sup> Andrew Ozarowski,<sup>e</sup> J. Krzystek<sup>e</sup>

<sup>a</sup> Department of Chemistry, University of Central Arkansas, Conway, Arkansas 72035

<sup>b</sup> EOIR Technologies, Lorton, Virginia 22079

<sup>c</sup> Max-Planck Institute for Bioinorganic Chemistry, Stiftstrasse 34-36, D-45470 Mülheim an der Ruhr, Germany

<sup>d</sup> Department of Biological, Chemical and Physical Sciences, Roosevelt University, Chicago, Illinois 60605

<sup>e</sup> National High Magnetic Field Laboratory, Florida State University, Tallahassee, Florida 32310

\* Corresponding authors e-mail: [patrickd@uca.edu](mailto:patrickd@uca.edu) (PD), [jtelser@roosevelt.edu](mailto:jtelser@roosevelt.edu) (JT)

## CONTENTS:

Ligand-Field Analysis of $\text{Tp}^*\text{NiBH}_4$ for Quantum Chemical Calculations.....	S3
Table S1: Metrical parameters for AOM analysis of $\text{Tp}^*\text{NiBH}_4$ .....	S7
Table S2: Calculated energies for key d-d excited states in $\text{Tp}^*\text{NiBH}_4$ and their corresponding contributions to $D^{\text{SOC}}$ .....	S8
Figure S1: Visible-near-infrared electronic spectra of $\text{Tp}^*\text{NiBH}_4$ in $\text{CD}_2\text{Cl}_2$ solution and as a solid using diffuse reflectance.....	S9
Figure S2: HFEPR spectral comparison of $\text{Tp}^*\text{NiBH}_4$ and $\text{Tp}^*\text{NiBD}_4$ recorded at 442 GHz.....	S10
Figure S3: HFEPR spectrum of $\text{Tp}^*\text{NiBD}_4$ recorded at 281.49 GHz.....	S11
Figure S4: Resonance field vs. frequency dependence for $\text{Tp}^*\text{NiBD}_4$ .....	S12
Figure S5: Qualitative MO descriptions of borohydride ion in $T_d$ and $C_{3v}$ symmetry.....	S13
Figure S6: Comparison of infrared spectra of $\text{Tp}^*\text{ZnBH}_4$ and $\text{Tp}^*\text{ZnBD}_4$ in $\text{CH}_2\text{Cl}_2$ solution.....	S14
Figure S7: Expansion of $\nu(\text{B-H})$ region in infrared spectra of $\text{Tp}^*\text{NiBD}_4$ and $\text{Tp}^*\text{NiBH}_4$ in $\text{CH}_2\text{Cl}_2$ solution.....	S15
Figure S8: $^1\text{H}$ NMR spectrum of $\text{Tp}^*\text{ZnBH}_4$ .....	S16
Figure S9: $^{13}\text{C}$ NMR spectrum of $\text{Tp}^*\text{ZnBH}_4$ .....	S17
Figure S10: Expansion of $\delta(\text{BD}_4)$ region in $^2\text{H}$ NMR spectrum of $\text{Tp}^*\text{ZnBD}_4$ in $\text{CD}_2\text{Cl}_2$ solution.....	S18
Figure S11: Expansion of $\delta(\text{BD}_4)$ region in $^{11}\text{B}$ NMR spectrum of $\text{Tp}^*\text{ZnBD}_4$ in $\text{CD}_2\text{Cl}_2$ solution.....	S19
Figure S12: MO diagram of $\text{Tp}^*\text{ZnBH}_4$ .....	S20

## Ligand-Field Analysis of $\text{Tp}^*\text{NiBH}_4$ for Quantum Chemical Calculations

A ligand-field analysis was carried out first in order to understand fully the physical origin of the zfs in  $\text{Tp}^*\text{NiBH}_4$ . To take the mixing of the two e-sets (1e and 2e) into account, the Ni-3d based MOs can be written as:

$$\begin{aligned}
 2a_1 &\cong \beta_{z^2} d_{z^2}; \\
 1e_{x^2-y^2} &\cong \alpha_{x^2-y^2, xy} d_{x^2-y^2} + \alpha_{xz, yz} d_{yz}; \\
 1e_{xy} &\cong \alpha_{x^2-y^2, xy} d_{xy} + \alpha_{xz, yz} d_{xz}; \\
 2e_{xz} &\cong \gamma_{xz, yz} d_{xz} + \gamma_{x^2-y^2, xy} d_{xy}; \\
 2e_{yz} &\cong \gamma_{xz, yz} d_{yz} + \gamma_{x^2-y^2, xy} d_{x^2-y^2}.
 \end{aligned} \tag{1}$$

The importance of this mixing will be shown below. The wavefunctions used in the ligand field treatment are the following:

$$\begin{aligned}
 |^3A_2(\text{g.s.})\rangle &= |(core)2e_{xz} 2e_{yz}| \\
 |^1A_1(2e \rightarrow 2e)\rangle &= \frac{1}{\sqrt{2}} (|(core)2e_{xz} \overline{2e_{xz}}| + |(core)2e_{yz} \overline{2e_{yz}}|) \\
 |^1E(2e \rightarrow 2e)\rangle &= \frac{1}{\sqrt{2}} (|(core)2e_{xz} \overline{2e_{xz}}| - |(core)2e_{yz} \overline{2e_{yz}}|) \\
 &\quad \frac{1}{\sqrt{2}} (|(core)2e_{xz} \overline{2e_{yz}}| - |(core)\overline{2e_{xz}} 2e_{yz}|) \\
 |^3A_1(1e \rightarrow 2e)\rangle &= \frac{1}{\sqrt{2}} (|(core)1e_{xz} 2e_{x^2-y^2}| - |(core)1e_{yz} 2e_{xy}|) \\
 |^3A_2(1e \rightarrow 2e)\rangle &= \frac{1}{\sqrt{2}} (|(core)1e_{xy} 2e_{xz}| + |(core)1e_{x^2-y^2} 2e_{yz}|) \\
 |^3E(1e \rightarrow 2e)\rangle &= \frac{1}{\sqrt{2}} (|(core)1e_{x^2-y^2} 2e_{xz}| + |(core)1e_{xy} 2e_{yz}|) \\
 &\quad \frac{1}{\sqrt{2}} (|(core)1e_{xy} 2e_{xz}| - |(core)1e_{x^2-y^2} 2e_{yz}|)
 \end{aligned} \tag{2}$$

$$|^3E(2a_1 \rightarrow 2e)\rangle = \frac{|(core)2a_1 2e_{xz}\rangle}{|(core)2a_1 2e_{yz}\rangle}$$

Orbitals with an over-bar are occupied with a spin-down electron,  $|\dots\rangle$  denotes a normalized Slater determinant, and  $(core)$  represents the inactive doubly occupied MOs of the system. For clarity, only the singly occupied Ni-3d based MOs are explicitly indicated in the Slater determinant, and the remaining doubly occupied Ni-3d based MOs are omitted.

Using the ligand field type arguments elaborated elsewhere,<sup>1</sup> one may readily obtain:

$$D^{SOC}(^3A_2) \cong \zeta_{Ni}^2 \left[ \frac{\left( \alpha_{xz,yz}^2 - 2\alpha_{xy,x^2-y^2}^2 \right)^2}{\Delta(^1A_1(2e \rightarrow 2e))} + \frac{3}{4} \frac{\beta_z^2 \gamma_{xz,yz}^2}{\Delta(^3E(2a_1 \rightarrow 2e))} - \frac{3}{4} \frac{\beta_z^2 \gamma_{xz,yz}^2}{\Delta(^1E(2a_1 \rightarrow 2e))} \right. \\ - \frac{1}{2} \frac{\left( 2\alpha_{xy,x^2-y^2} \gamma_{xy,x^2-y^2} - \alpha_{xz,yz} \gamma_{xz,yz} \right)^2}{\Delta(^3A_1(1e \rightarrow 2e))} + \frac{1}{2} \frac{\left( 2\alpha_{xy,x^2-y^2} \gamma_{xy,x^2-y^2} - \alpha_{xz,yz} \gamma_{xz,yz} \right)^2}{\Delta(^1A_1(1e \rightarrow 2e))} \\ \left. + \frac{1}{2} \frac{\left( \alpha_{xy,x^2-y^2} \gamma_{xz,yz} - \alpha_{xz,yz} \gamma_{xy,x^2-y^2} \right)^2}{\Delta(^3E(1e \rightarrow 2e))} - \frac{1}{2} \frac{\left( \alpha_{xy,x^2-y^2} \gamma_{xz,yz} - \alpha_{xz,yz} \gamma_{xy,x^2-y^2} \right)^2}{\Delta(^1E(1e \rightarrow 2e))} \right] \quad [3]$$

Here,  $\zeta_{Ni}$  is the one-electron SOC constant for a Ni-3d electron,  $\alpha_i^2$ ,  $\beta_i^2$ , and  $\gamma_i^2$  are the nickel characters of the indicated type in the metal-d based MOs (Equation 1), and  $\Delta(X)$  is the transition energy from the  $^3A_2$  ground state to excited state X.

The contribution from each excited state to the total  $D$  value is given in Table S2 and can be estimated using the transition energies,  $\Delta(X)$ , obtained from the *ab initio* calculations and the computed SOC matrix elements. These computed  $\Delta(X)$  (see Table 2) are in reasonable agreement with the available experimental data. As anticipated, the largest magnitude contributions come from the lowest lying triplet excited states; however, these values are opposite in sign. Importantly, the contributions from spin-flip transitions (singlet excited states)

account for more than 20% of the sum of the absolute values for all excited states and are therefore not negligible, in contrast to many simple LFT models that consider only same spin transitions.

Indeed, inspection of Equation 3 shows that when a given triplet excited state makes a contribution to  $D$ , then its singlet partner with the same space part but distinct spin coupling will deliver an opposite sign contribution to  $D$ . However, the intra-SOMO spin-flip transition,  $^1A_1(2e \rightarrow 2e)$ , has no triplet counterpart, so it gives an unopposed positive contribution.<sup>2</sup> In order to predict accurate  $D$  values, one thus has to calculate small differences among several contributions of similar magnitudes, varying signs, and of different physical origins – which must be properly described.

This challenge can be demonstrated by the following illustrative example. The contributions to  $D^{\text{SOC}}$  from  $^3A_1(1e \rightarrow 2e)$  and  $^1A_1(1e \rightarrow 2e)$  originate from the mixing of the two e-sets. If this mixing is ignored, then  $\alpha_{xz,yz}$  and  $\gamma_{xy,x^2-y^2}$  in Equation 3 are taken to be zero (see also Equation 1), and the terms for both of these excited states will vanish. This will lead to Equation 4, where assuming no mixing allows a further approximation of the wavefunction coefficients as unity:

$$\begin{aligned}
D^{\text{SOC}}(^3\text{A}_2) &\cong \\
&\zeta_{\text{Ni}}^2 \left[ \frac{\left(-2\alpha_{xy,x^2-y^2}^2\right)^2}{\Delta(^1\text{A}_1(2e \rightarrow 2e))} + \frac{3}{4} \frac{\beta_{\xi^2}^2 \gamma_{xz,yz}^2}{\Delta(^3\text{E}(2a_1 \rightarrow 2e))} - \frac{3}{4} \frac{\beta_{\xi^2}^2 \gamma_{xz,yz}^2}{\Delta(^1\text{E}(2a_1 \rightarrow 2e))} \right. \\
&\quad \left. + \frac{1}{2} \frac{\left(\alpha_{xy,x^2-y^2} \gamma_{xz,yz}\right)^2}{\Delta(^3\text{E}(1e \rightarrow 2e))} - \frac{1}{2} \frac{\left(\alpha_{xy,x^2-y^2} \gamma_{xz,yz}\right)^2}{\Delta(^1\text{E}(1e \rightarrow 2e))} \right] \\
&\approx \frac{1}{4} \zeta_{\text{Ni}}^2 \left[ \frac{16}{\Delta(^1\text{A}_1(2e \rightarrow 2e))} + \frac{3}{\Delta(^3\text{E}(2a_1 \rightarrow 2e))} - \frac{3}{\Delta(^1\text{E}(2a_1 \rightarrow 2e))} \right. \\
&\quad \left. + \frac{2}{\Delta(^3\text{E}(1e \rightarrow 2e))} - \frac{2}{\Delta(^1\text{E}(1e \rightarrow 2e))} \right] \quad [4]
\end{aligned}$$

This approximation seems attractive as a method for providing an estimate as to the origin of  $D$ , but it is very dangerous. As seen from Table S2, although eliminating the contribution to  $D^{\text{SOC}}$  from  $^1\text{A}_1(1e \rightarrow 2e)$  is indeed insignificant, eliminating that from  $^3\text{A}_1(1e \rightarrow 2e)$  is not. Use of Equation 4 would give a very large magnitude positive  $D$  value; very different from experiment.

## References

1. Neese, F.; Solomon, E. I., In *Magnetoscience - From Molecules to Materials*, Miller, J. S.; Drillon, M., Eds. Wiley: New York, 2003; Vol. IV, pp 345-466.
2. Ye, S.; Neese, F.; Ozarowski, A.; Smirnov, D.; Krzystek, J.; Telser, J.; Liao, J.-H.; Hung, C.-H.; Chu, W.-C.; Tsai, Y.-F.; Wang, R.-C.; Chen, K.-Y.; Hsu, H.-F. *Inorg. Chem.* **2010**, *49*, 977-988.

**Table S1.** Metrical parameters for AOM analysis of Tp\*NiBH<sub>4</sub>.

N-donor Bond Angles <sup>a</sup>	Experimental Angle (deg)	$\theta$ (deg) used for AOM
B2-Ni-N1	123.54	N1: 123.54
B2-Ni-N3	123.20	N3: 123.20
B2-Ni-N5	127.37	N5: 127.37
average value	124.70	

N-donor Torsional Angles <sup>b</sup>	Experimental Angle (deg)	$\phi$ (deg) used for AOM
N1-B1-Ni-N4	120.49	N1: 0
N2-B1-Ni-N3	120.14	N3: 120
N1-B1-Ni-N6	119.96	
N2-B1-Ni-N5	119.82	N5: 240
N3-B1-Ni-N6	119.95	
N4-B1-Ni-N5	119.63	
average value	120.00	

H-donor Bond Angles <sup>c</sup>	Experimental Angle (deg)	$\theta$ (deg) used for AOM
B2-Ni-H23	32.93	H23: 34
B2-Ni-H24	34.79	H24: 34
B2-Ni-H26	34.38	H26: 34
average value	34.03	
H-donors Angles for AOM <sup>d</sup>		$\phi$ (deg) used for AOM
		H23: 60
		H24: 180
		H26: 300

<sup>a</sup> Atom labels are defined in the figure below. The B1-Ni-B2 bond angle is 177.46°, which is sufficiently close to 180° that the B2-Ni vector is used to define the molecular  $z$  ( $C_3$  axis) for the AOM analysis. The individual experimental  $\theta$  values for the three N-donors (N1, N3, N5) were used for the AOM analysis.

<sup>b</sup> The variation in  $\phi$  angle is so small for the Tp\* N ligands and the average value is indeed ideal three-fold symmetry, so that ideal  $\phi$  values were used for N1, N3, N5 in the AOM analysis, with the Ni-N1 vector defined as the molecular  $x$  axis.

<sup>c</sup> The average value of 34.0° was used for all of the  $\theta$  angles for the borohydride  $\kappa^3$ -H ligands

<sup>d</sup> Idealized three-fold symmetry is assumed for all of the  $\phi$  angles for the  $\kappa^3$ -H ligands.

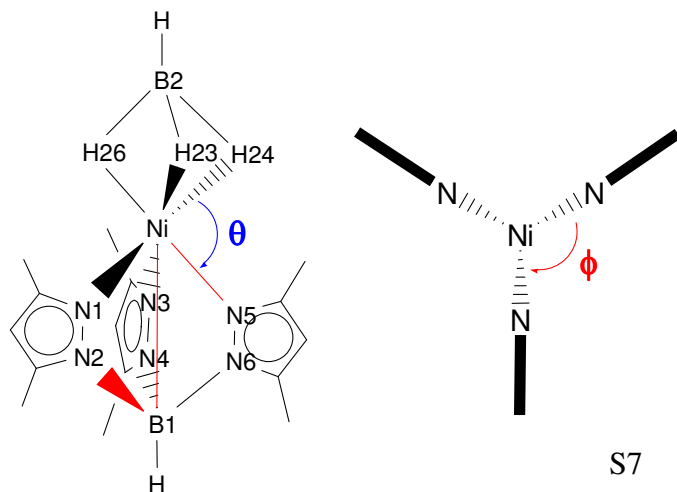


**Table S2.** Calculated energies for key d-d excited states in Tp\*NiBH<sub>4</sub> (experimental data in parentheses) and their corresponding contributions to  $D^{\text{SOC}}$ .<sup>a</sup>

Method	CASSCF		NEVPT2	
State	Energy (cm <sup>-1</sup> )	Contribution to $D$ (cm <sup>-1</sup> )	Energy (cm <sup>-1</sup> )	Contribution to $D$ (cm <sup>-1</sup> )
<sup>1</sup> A <sub>1</sub> (2e→2e)	24660	+14.4	26310	+13.5
<sup>1</sup> E (2e→2e)	17730	0	15710	0
<sup>3</sup> A <sub>1</sub> (1e→2e)	7110	-52.6	10600	-36.0
<sup>1</sup> A <sub>1</sub> (1e→2e)	28450	+0.1	27350	+0.1
<sup>3</sup> E (1e→2e)	7660 (9400)	+53.3	11260 (9400)	+37.1
<sup>1</sup> E (1e→2e)	24380	-14.0	25980	-13.2
<sup>3</sup> A <sub>2</sub> (1e→2e)	11560	0	16270	0
<sup>3</sup> E (2a <sub>1</sub> →2e)	13680 (13700)	+0.2	19770 (13700)	+0.2
<sup>1</sup> E (2a <sub>1</sub> →2e)	31470	-0.2	32680	-0.2
<sup>3</sup> E (1e→2e, 2a <sub>1</sub> →2e)	27890 (24400)	0	29420 (24400)	0
<sup>3</sup> A <sub>2</sub> (1e→2e, 1e→2e)	28400	0	30660	0
Total $D^{\text{SOC}}$		+1.2		+1.5

<sup>a</sup> Idealized octahedral symmetry is mapped onto the real symmetry using the following compatible rules (noting that there is severe mixing of states with the same symmetry so that a given state may contain the contributions from several ligand-field configurations):

$${}^3T_{2g}(\text{F})(t_2^5e^3) + {}^3T_{1g}(\text{F})(t_2^5e^3) \rightarrow {}^3A_1(1e \rightarrow 2e) + {}^3A_2(1e \rightarrow 2e) + {}^3E(1e \rightarrow 2e) + {}^3E(2a_1 \rightarrow 2e)$$

$${}^1E_{1g}(\text{D})(t_2^6e^2) \rightarrow {}^1E(2e \rightarrow 2e)$$

$${}^1A_{1g}(\text{G})(t_2^6e^2) \rightarrow {}^1A_1(2e \rightarrow 2e)$$

$${}^1T_{2g}(\text{D})(t_2^5e^3) + {}^1T_{2g}(\text{G})(t_2^5e^3) \rightarrow {}^1A_1(1e \rightarrow 2e) + {}^1A_2(1e \rightarrow 2e) + {}^1E(1e \rightarrow 2e) + {}^1E(2a_1 \rightarrow 2e)$$

$${}^3T_{1g}(\text{F})(t_2^4e^4) \rightarrow {}^3A_2(1e \rightarrow 2e, 1e \rightarrow 2e) + {}^3E(1e \rightarrow 2e, 2a_1 \rightarrow 2e)$$



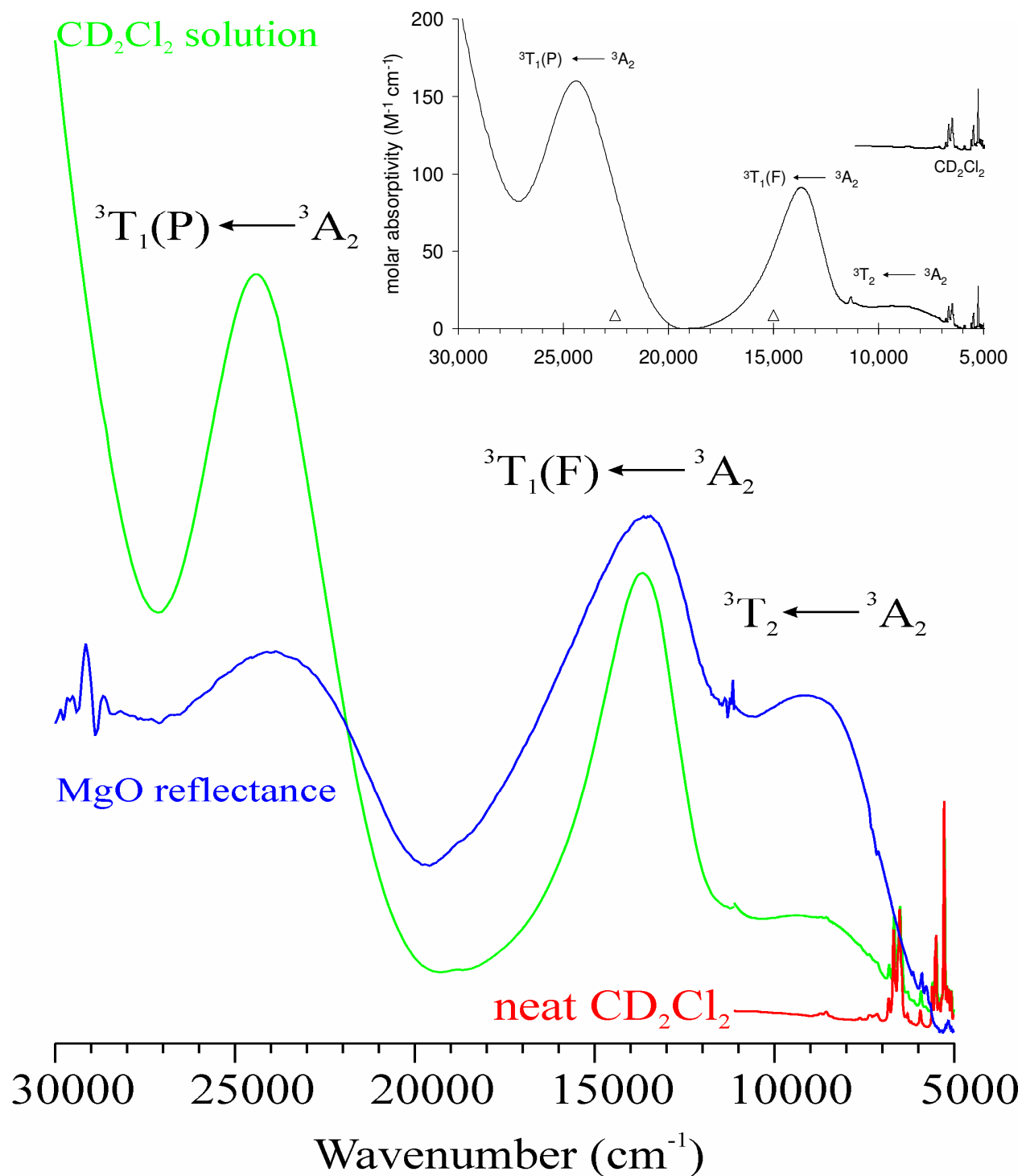


**Figure S1.** Visible-near-infrared electronic spectrum of Tp\*NiBH<sub>4</sub> recorded as both a CD<sub>2</sub>Cl<sub>2</sub> solution (green trace) and using diffuse reflectance (blue trace) with MgO as a reference. The near-infrared spectrum of CD<sub>2</sub>Cl<sub>2</sub> is shown at lower right (red trace). The intensity scaling is arbitrary, but the inset shows the solution spectrum with the ordinate in molar absorptivity (M<sup>-1</sup> cm<sup>-1</sup>). The triangles in the inset indicate spin-forbidden transitions. These data indicate nearly identical electronic structures for Tp\*NiBH<sub>4</sub> in the solid state and in solution.

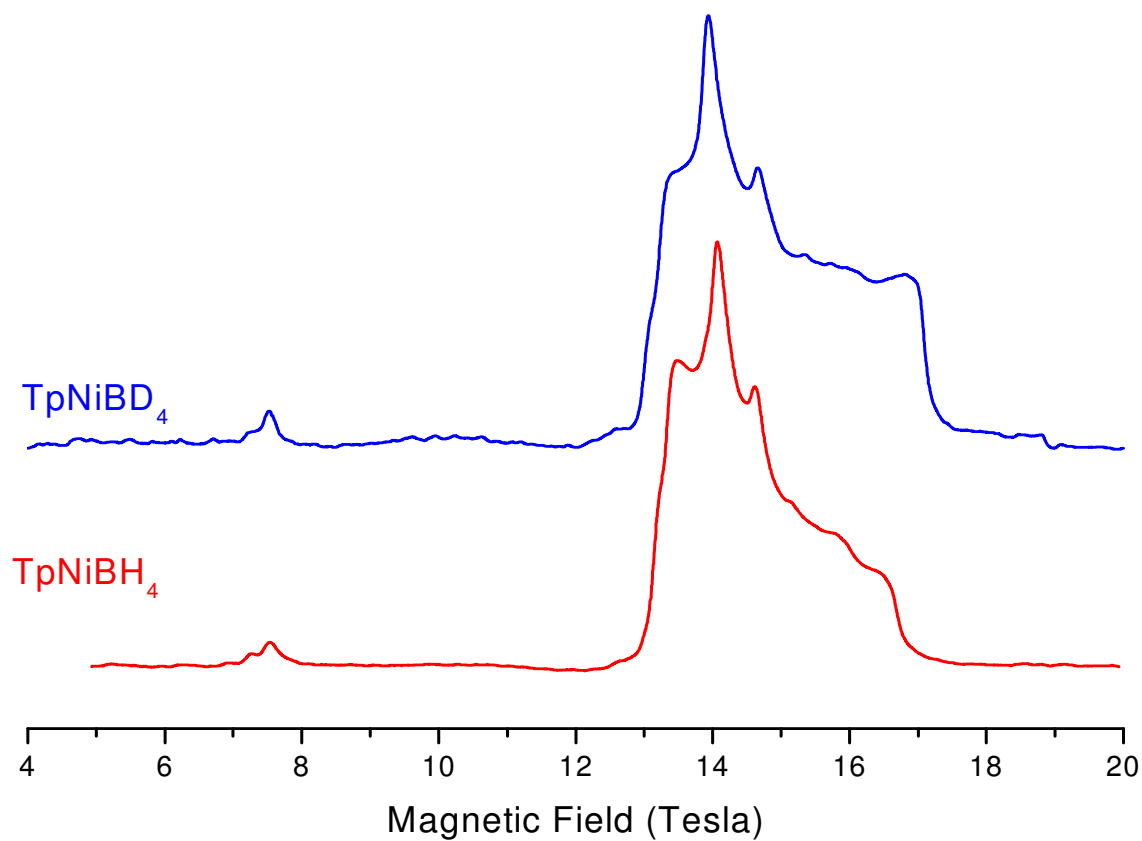


**Figure S2.** HFEPR spectra of solid Tp\*NiBH<sub>4</sub> (red trace) and Tp\*NiBD<sub>4</sub> (blue trace), each recorded at 5.6 K in the resistive magnet using a BWO source operating at 442 GHz, and an optical modulation (chopping the sub-THz wave beam), resulting in the absorption shape.

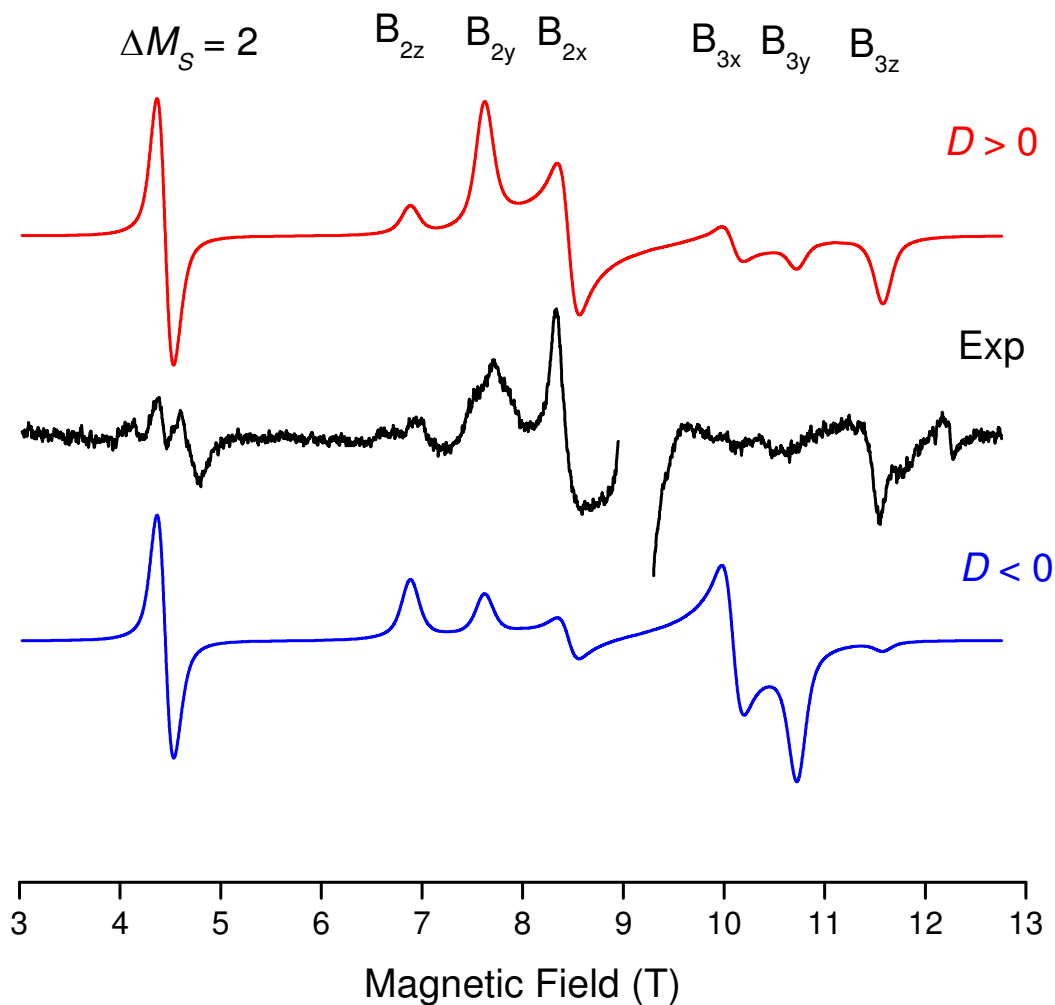


**Figure S3.** HFEPR spectrum of solid Tp\*NiBD<sub>4</sub> at 281.49 GHz and 10 K. The black trace is experiment while the colored lines were simulated using the following spin-Hamiltonian parameters:  $S = 1$ ,  $|D| = 2.38 \text{ cm}^{-1}$ ,  $|E| = 0.25 \text{ cm}^{-1}$ ,  $g_{x,y} = 2.15$ ,  $g_z = 2.18$ . The red trace was simulated with positive zfs parameters; the blue trace with negative ones. Specific turning points in the recorded spectrum are labeled. The very intense double-quantum (DQ) resonance ( $\sim 9.2 \text{ T}$ ,  $g \approx 2.18$ ) was left out of the experimental trace and is not simulated.

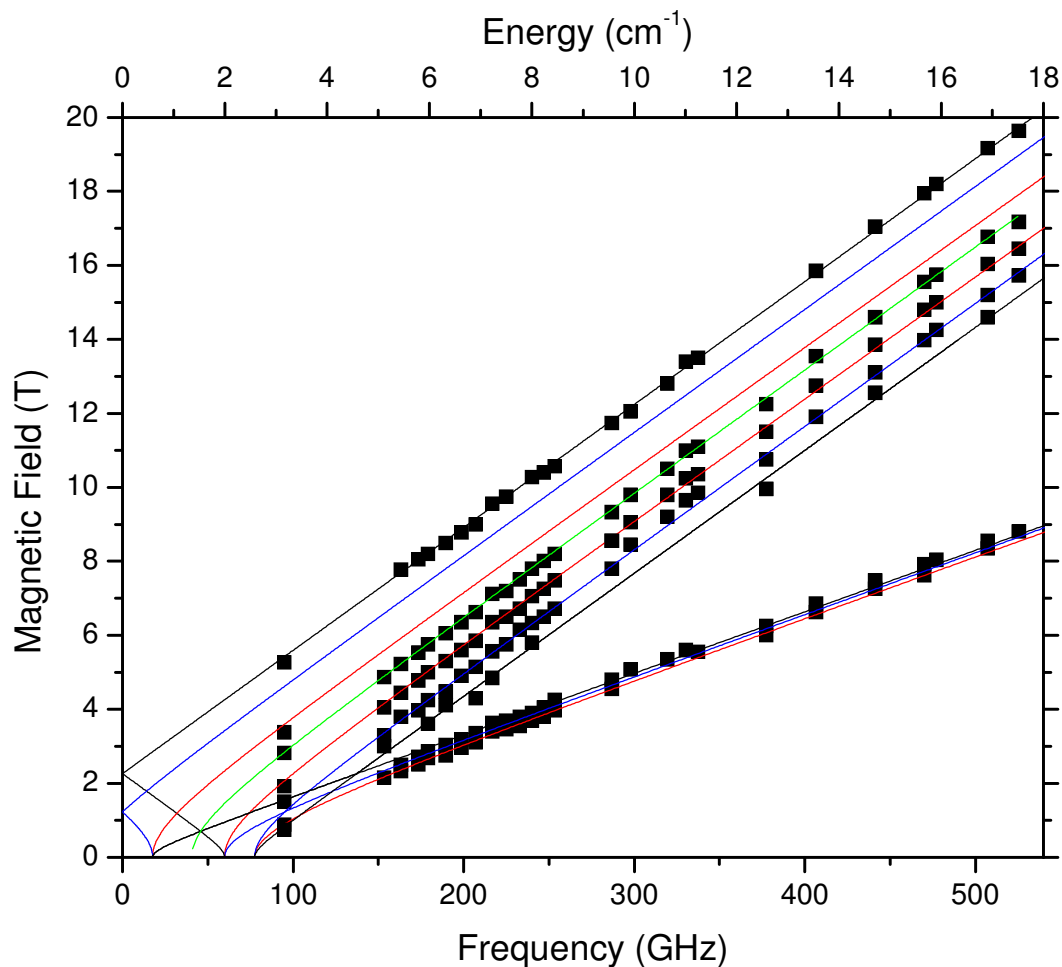


**Figure S4.** Resonance field vs. frequency (quantum energy) dependence for  $\text{Tp}^*\text{NiBD}_4$  at 4.5 K. Squares are experimental data; curves are simulated using parameters as in Table 1: red lines are  $B_0 \parallel x$  turning points; blue lines are  $B_0 \parallel y$  turning points; black lines are  $B_0 \parallel z$  turning points; the green line is the double-quantum transition.

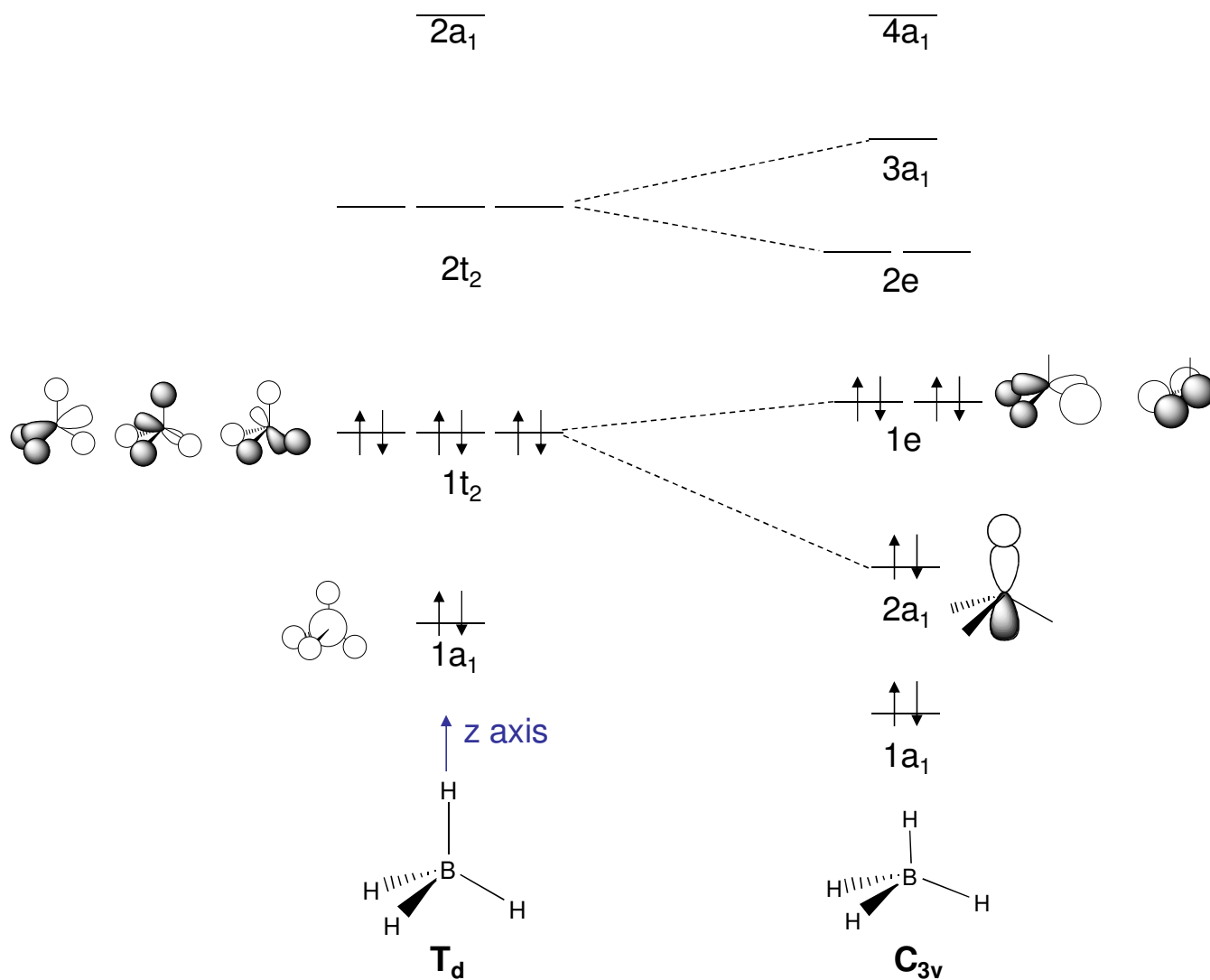


**Figure S5.** Qualitative MO descriptions of borohydride ion in  $T_d$  symmetry (left) and in  $C_{3v}$  symmetry (right). The left diagram is for free  $\text{BH}_4^-$  ion and the right diagram results from a trigonal compression along one of the B-H vectors, which would result from  $\kappa^3$ -coordination, as in  $\text{Tp}^*\text{Ni}(\kappa^3\text{-BH}_4)$ . The frontier  $1e$  and  $2a_1$  MO's of the compressed borohydride match those responsible for most of the covalent nickel-borohydride interaction represented in Figure 4 (MO's  $1a_1$ ,  $2a_1$ , and  $2e$ ).

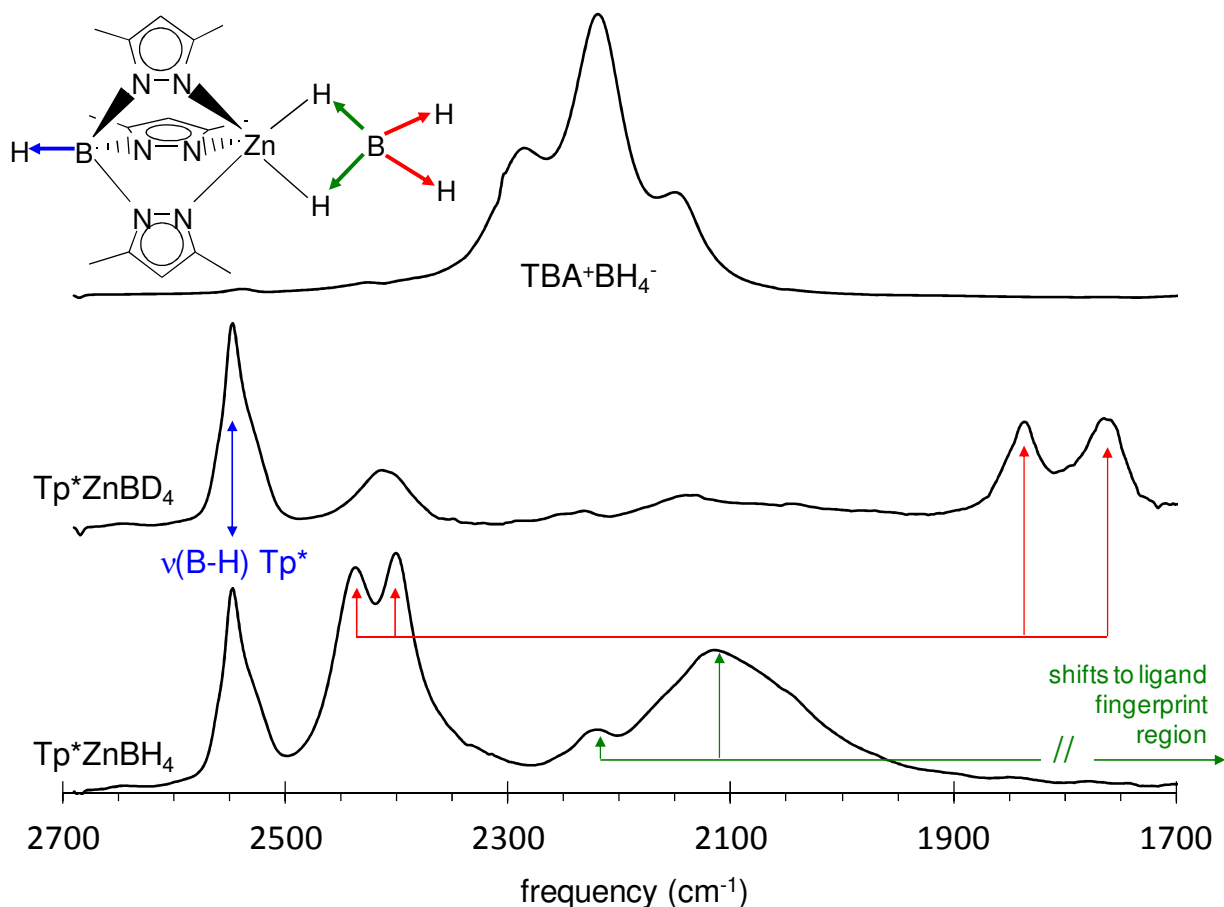


**Figure S6.** Infrared spectra of  $\text{Tp}^*\text{Zn}(\kappa^2\text{-BH}_4)$  (bottom),  $\text{Tp}^*\text{Zn}(\kappa^2\text{-BD}_4)$  (middle), and tetra-*n*-butylammonium (TBA) borohydride (top) in  $\text{CH}_2\text{Cl}_2$  solution (50 mM each). The vibration assigned to  $\nu(\text{B-H}_t)$  ( $t$  = terminal; red arrows) is resolved as a pair of bands at 2400 – 2450  $\text{cm}^{-1}$  that shifts to a pair at 1750 – 1850  $\text{cm}^{-1}$  as  $\nu(\text{B-D}_t)$ . The vibration assigned to  $\nu(\text{B-H}_b)$  ( $b$  = bridging; green arrows) shifts out of range for  $\nu(\text{B-D}_b)$ . The persistent ligand  $\nu(\text{B-H})$  band (blue arrows) is seen unshifted in both Zn complex spectra. These spectra show the  $\nu(\text{B-H})$  pattern expected for  $\kappa^2$  borohydride coordination, observed in the solid state (Figure 5), persists in solution.

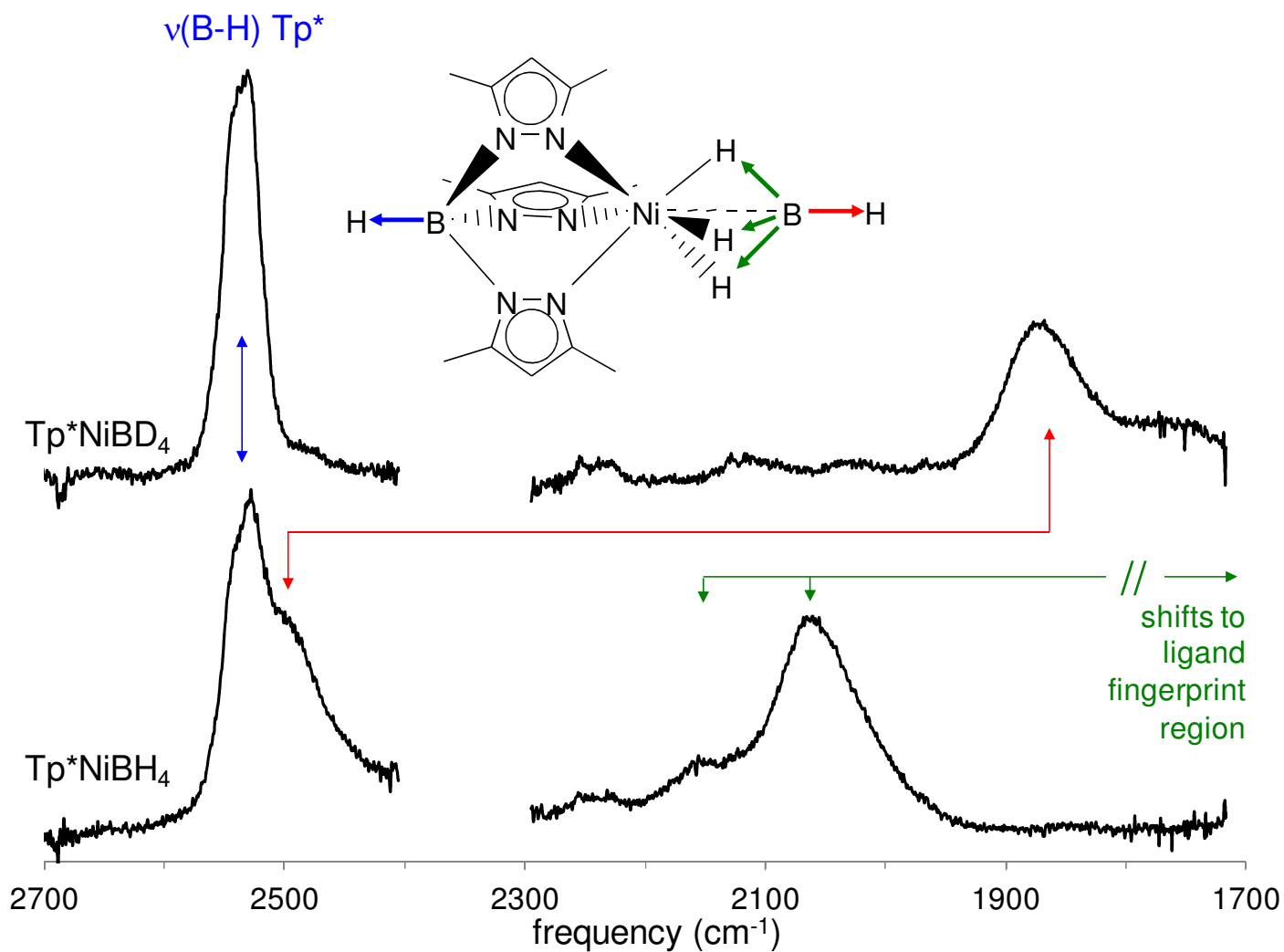


**Figure S7.** Infrared spectra of  $\text{Tp}^*\text{NiBD}_4$  (top) and  $\text{Tp}^*\text{NiBH}_4$  (bottom) in  $\text{CH}_2\text{Cl}_2$  solution (50 mM). The region from 2300 – 2400  $\text{cm}^{-1}$  is obscured by intense ligand overtone and ambient background noise and is omitted for clarity. The vibration assigned to  $\nu(\text{B-H}_t)$  ( $t$  = terminal; red arrows) is resolved as a shoulder near 2500  $\text{cm}^{-1}$  that shifts to near 1870  $\text{cm}^{-1}$  as  $\nu(\text{B-D}_t)$ . The vibration assigned to  $\nu(\text{B-H}_b)$  ( $b$  = bridging; green arrows) shifts out of range for  $\nu(\text{B-D}_b)$ . The persistent ligand  $\nu(\text{B-H})$  band (blue arrows) is seen unshifted in both spectra.

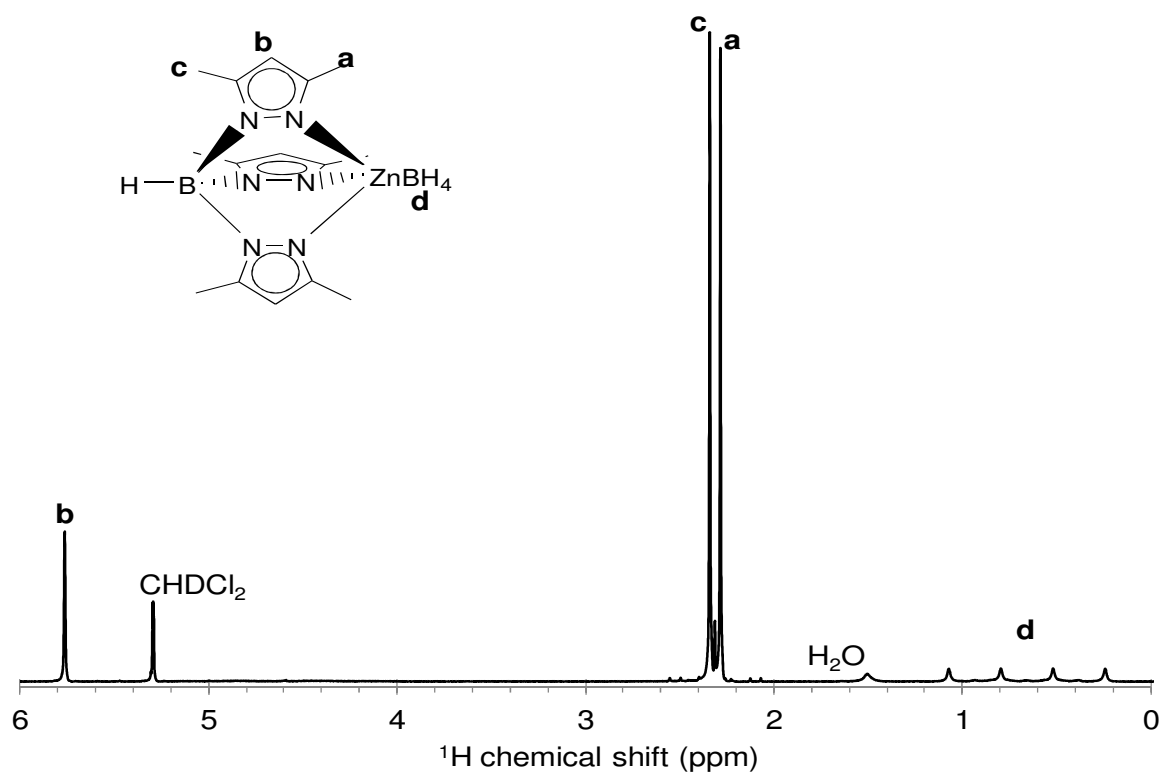


**Figure S8.**  $^1\text{H}$  NMR spectrum of  $\text{Tp}^*\text{ZnBH}_4$  in  $\text{CD}_2\text{Cl}_2$ .



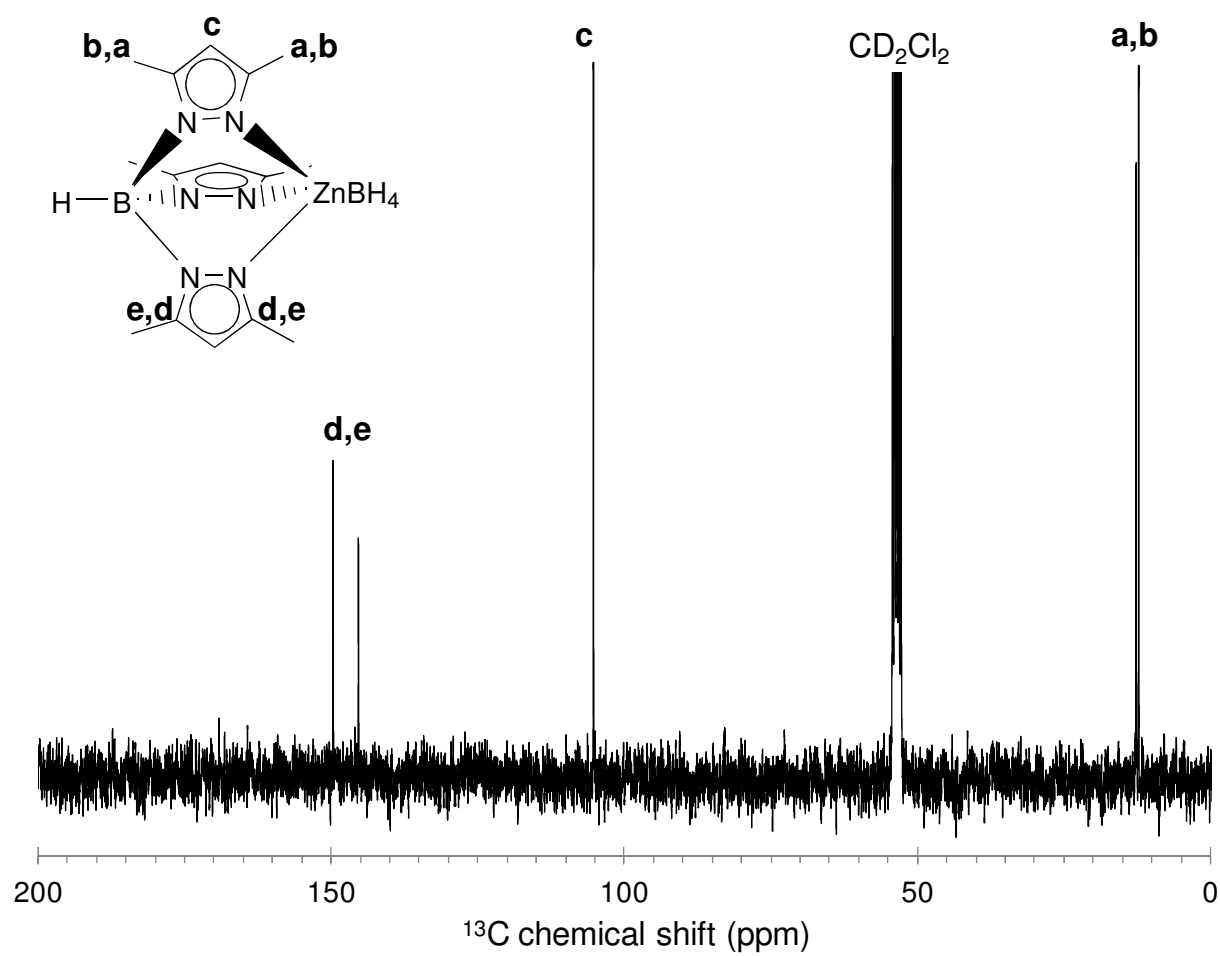


**Figure S9.**  $^{13}\text{C}\{^1\text{H}\}$  NMR spectrum of  $\text{Tp}^*\text{ZnBH}_4$  in  $\text{CD}_2\text{Cl}_2$ .

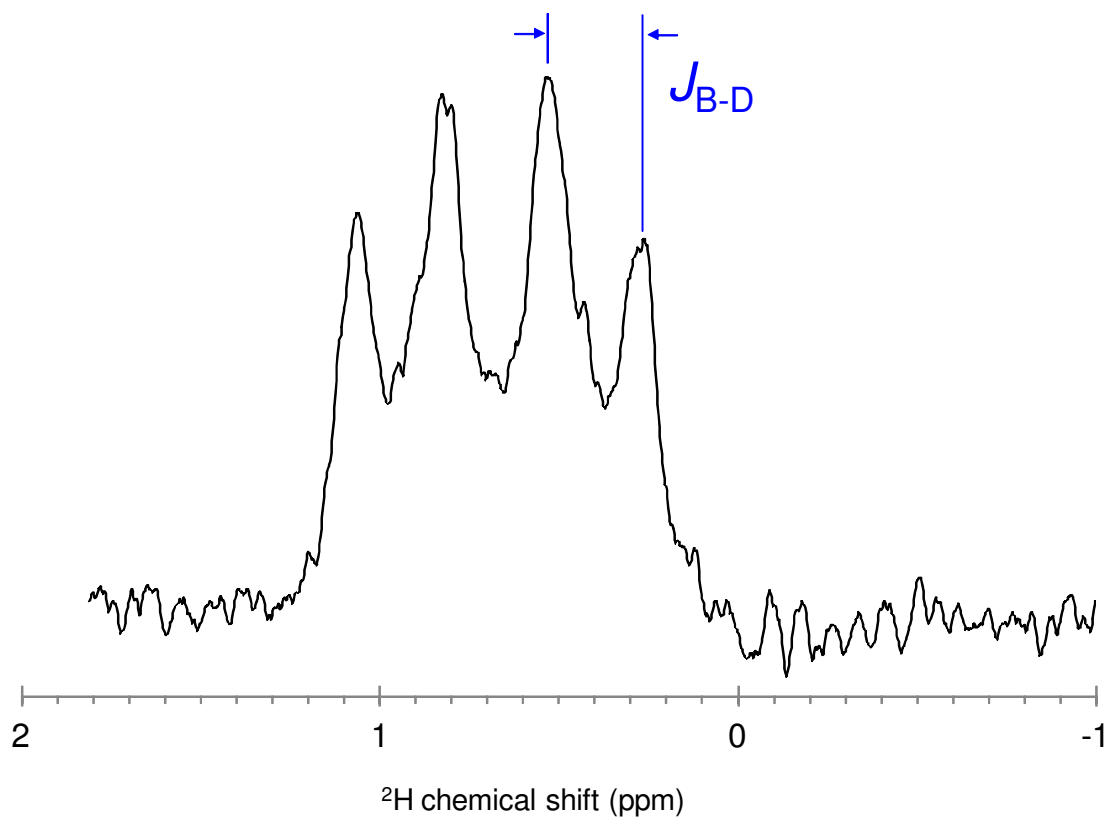


**Figure S10.** Expansion of  $^2\text{H}$  NMR spectrum of  $\text{Tp}^*\text{ZnBD}_4$  in  $\text{CD}_2\text{Cl}_2$  ( $\delta = 5.32$  ppm) showing the quartet assigned to  $\text{BD}_4$ , with  $J_{\text{B-D}} = 12$  Hz.

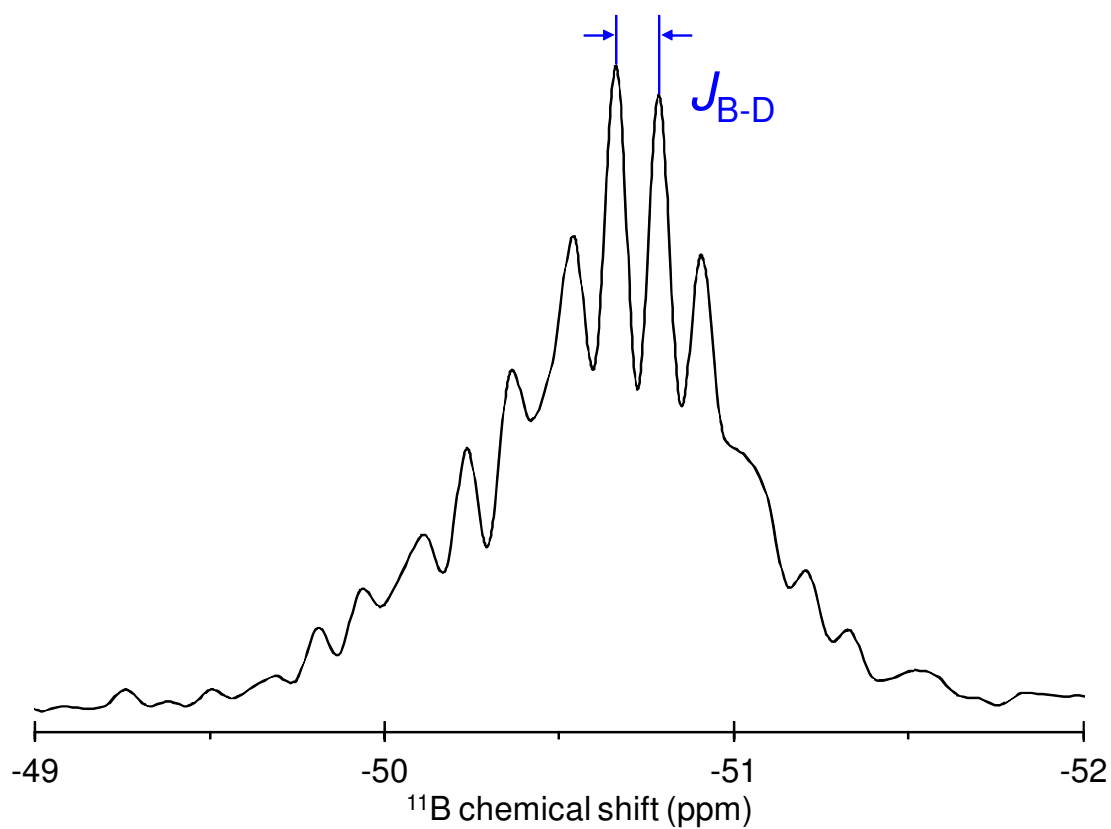


**Figure S11.** Expansion of  $^{11}\text{B}$  NMR spectrum of  $\text{Tp}^*\text{ZnBD}_4$  in  $\text{CD}_2\text{Cl}_2$  showing the multiplet (ideally, a nonet with intensities 1:3:6:9:10:9:6:3:1) assigned to  $\text{BD}_4$ , with  $J_{\text{B-D}} = 12$  Hz. See Figure 7 for complete spectrum. The non-first-order pattern is likely the result of nuclear quadrupole coupling effects in both  $^2\text{H}$  ( $I = 1$ ) and  $^{11}\text{B}$  ( $I = 3/2$ ).

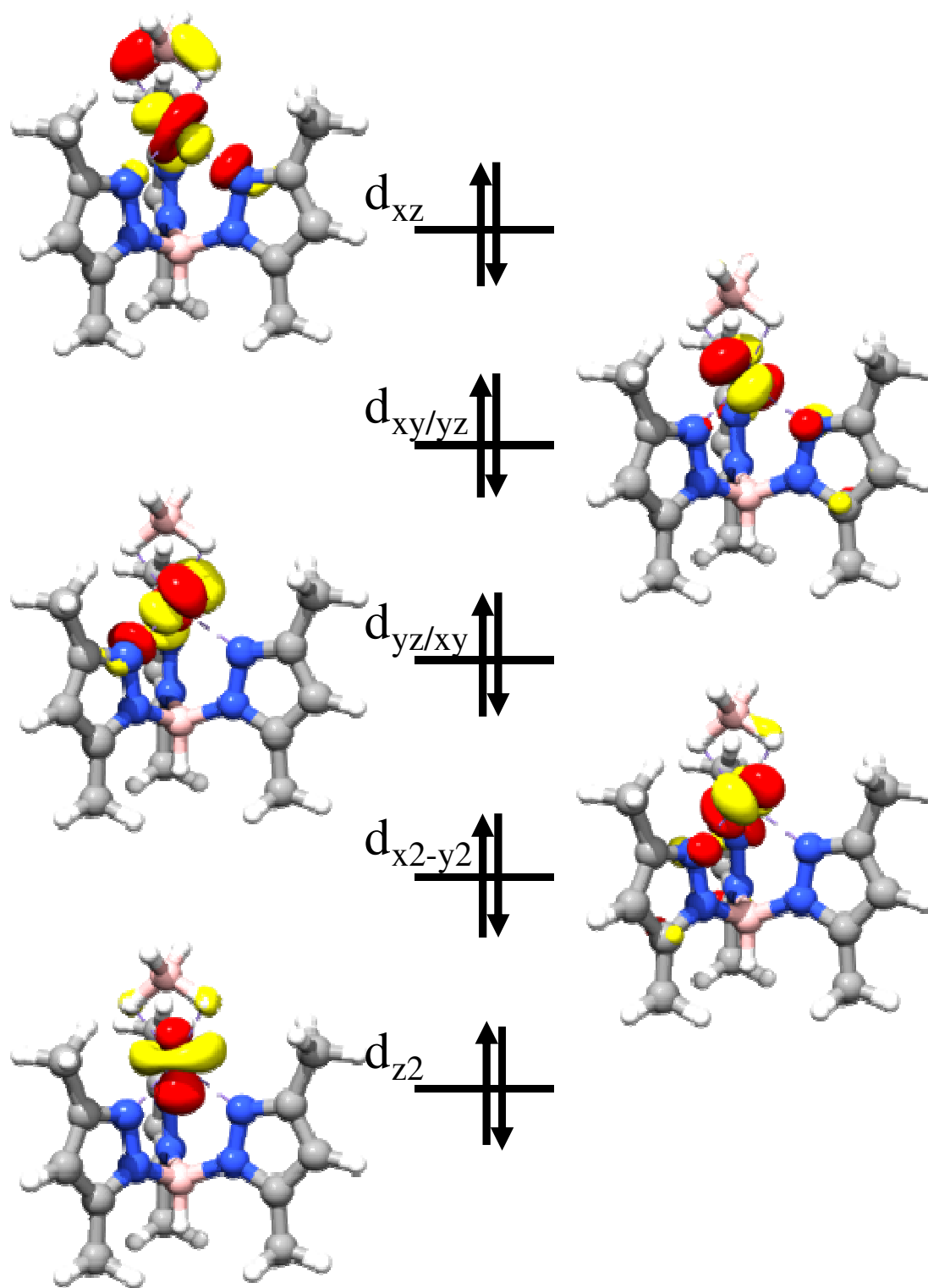


**Figure S12.** MO diagram of  $\text{Tp}^*\text{ZnBH}_4$ . The interaction of the  $\kappa^2$ -coordinated  $\text{BH}_4^-$  ligand with the metal center is strikingly different from that involving a  $\kappa^3$ -coordinated  $\text{BH}_4^-$  (Figure 4). There is only one  $\pi$ -bond as compared to two as observed in the nickel congener. More importantly, the metal-boron  $\sigma$ -type interaction completely disappears due to the unfavorable coordination geometry.